

# Microstructural Evolution of Polycrystalline Ice During Confined Creep Testing

Daniel J. Breton<sup>a,\*</sup>, Ian Baker<sup>b</sup>, David M. Cole<sup>a</sup>

<sup>a</sup>*Cold Regions Research and Engineering Laboratory, USA*

<sup>b</sup>*Thayer School of Engineering, Dartmouth College, USA*

---

## Abstract

The mechanical properties of polycrystalline ice  $I_h$  have been observed to change under an applied hydrostatic pressure comparable to that present near the bottom of kilometer-thick ice sheets. To determine the cause of these changes, we conducted confined creep testing of laboratory-prepared polycrystalline ice at pressures up to 20 MPa (simulating  $\sim 2000$  m of overburden) and subsequent microstructural analysis of specimens deformed by creep using optical microscopy and scanning electron microscopy, including extensive electron backscatter diffraction mapping of crystal orientations. Microstructural observations of the creep-deformed specimens revealed smaller mean grain sizes and less regular grain shapes in specimens deformed at higher pressure compared with those deformed at atmospheric pressure. Variable pressure testing reveals little change in strain rate for pressures less than 15 MPa, leading to new hypotheses regarding the influence of confining pressure on the creep behavior of polycrystalline ice. We present preliminary mechanical testing and microstructural data to support the notion that certain recovery and grain growth processes are enhanced

---

\*Corresponding author at: Cold Regions Research and Engineering Laboratory, 72 Lyme Road, Hanover, NH 03755, USA. Tel: +1 603 646 4197, Fax: +1 603 646 4644  
*Email address:* [daniel.j.breton@usace.army.mil](mailto:daniel.j.breton@usace.army.mil) (Daniel J. Breton)

within ice under terrestrially relevant pressures.

*Keywords:* creep, dislocation, electron backscatter diffraction, grain boundary, grain size, polycrystalline ice

---

## 1. Introduction

The effects of hydrostatic pressure on the creep properties of ice  $I_h$  are of interest for terrestrial ice sheet flow modeling and to gain fundamental insight into the structure of ice and its crystalline defects. Presently, ice sheets on Earth have maximum depths of  $\sim 3000$  m, yielding hydrostatic pressures  $P$  up to 30 MPa, and depressions of the melting temperature  $T_m$  down to  $-2.5^\circ\text{C}$  using the rate of  $-0.074^\circ\text{C MPa}^{-1}$  given in Hobbs (1974). The majority of laboratory experimental work has been performed within this range, both on single crystal and polycrystalline ice, and the work presented in this paper also focuses exclusively on the temperature and pressure range relevant to terrestrial ice. Following a review of the possible effects of hydrostatic pressure on creep and fabric development in ice, we review the experimental results to date to place this work in context.

### 1.1. Possible hydrostatic pressure effects on creep and relevant unique material characteristics of ice $I_h$

Steady state creep strain rate as a function of hydrostatic pressure is often described (Frost and Ashby, 1982) by

$$\dot{\epsilon} = A\sigma^n \exp\left[-\frac{E^* + PV^*}{k_B T}\right] \quad (1)$$

where  $A$  is a constant,  $\sigma$  is the applied non-hydrostatic stress,  $n$  is the creep exponent,  $E^*$  is the creep activation energy,  $V^*$  is the creep activation volume,  $k_B$  is Boltzmann's constant and  $T$  is the absolute temperature.

Because most crystalline materials exhibit  $V^* > 0$ , application of high pressure results in reduced rates of creep (Butcher and Ruoff, 1961; Sherby et al., 1970), slower grain growth (Hahn and Gleiter, 1979) and lower rates of recrystallization (Tanner and Radcliffe, 1962; Syrenko et al., 1973). In contrast, ice displays *negative* activation volumes for grain growth (Azuma and Higashi, 1983) and for creep at  $P > 10$  MPa (Jones and Chew, 1983b). The dominant point defect in ice is the interstitial (Hondoh et al., 1987) which increases in concentration with increasing  $P$ . Furthermore, ice has one of the lowest known stacking fault energies ( $\gamma_F$ ), a result of its open lattice and the very small energy difference between hexagonal and cubic ice structures (Hondoh, 2000). Keeping these unique characteristics in mind, we now examine the possible effects of pressure on creep and the development of fabric and texture in polycrystalline ice.

Following Poirier (1985), the possible effects of increased hydrostatic pressure on creep and fabric development include:

1. Resistance to dislocation formation and multiplication can occur with increasing  $P$ , as the presence of a dislocation represents a less perfect and therefore slightly higher volume crystal compared to similar defect-free crystal (Poirier, 1985). In some polycrystals with very large *elastic* anisotropy, dislocations and associated transient plastic flow can be generated under application of high  $P$  (Margevicius and Lewandowski, 1991) but this type of dislocation generation is negligible

for ice as it is nearly elastically isotropic (Schulson and Duval, 2009). Margevicius and Lewandowski characterized the relative isotropy of hexagonal materials via the ratio of  $c$ -axis to  $a$ -axis linear compressibilities,  $k_c/k_a$ . Using the compliance data of Gammon et al. (1983) for ice, we find  $k_c/k_a$  for ice is 1.14, compared with a value of 1.0 for a perfect elastically isotropic material, and a value of 8.7 for the highly anisotropic material cadmium.

2. Changes in dislocation production rate from Frank-Read sources can occur if the shear modulus  $G$  of the material changes with  $P$ . These sources have been observed to operate in single crystal ice (Ahmad et al., 1986), but are unimportant compared to the production of dislocations at grain boundaries (Liu et al., 1992, 1993). This effect is also likely negligible as  $G$  decreases by less than 0.2% from  $P = 0.1$  to 20 MPa (Helgerud et al., 2009), yet another unusual characteristic of ice compared to most materials whose shear moduli typically increase with  $P$ .
3. Strengths of dislocation-dislocation and dislocation-obstacle interactions are also expected to increase linearly with  $G$  (Hirth and Lothe, 1982). Given the negligible change in  $G$  with  $P$  for ice as discussed above, little change in the dislocation interaction strength is expected in ice.
4. The pressure dependence of the Peierls stress, or lattice friction, can also act to hinder the motion of dislocations under high pressure (Poirier, 1985). Peierls stress variation with  $P$  has not been quantified for ice, though it seems that the essentially null result of Cole

(1996) for basal slip and the noted absence of lattice friction for non-basal dislocations (Petrenko and Whitworth, 1999) suggests that this mechanism is unimportant for ice.

- 70
5. Dislocations in materials with low stacking fault energies often split into two partial dislocations bounding a ribbon of stacking fault between them (Hirth and Lothe, 1982). The width of these dissociated (or extended) dislocations can be described by  $w \propto G/(\gamma_F + \alpha P)$  where  $\alpha$  is a constant proportional to the lattice dilatation associated with the presence of the stacking fault (Fontaine and Haasen, 1969; Poirier, 1985). Increasing  $P$  will act to constrict dissociated dislocations and enhance the rate of recovery through dislocation climb and cross-slip (Weertman, 1965; Aladag et al., 1970; Nabarro, 2006). Given the extraordinarily low  $\gamma_F$  of ice, we expect that most dislocations are very widely extended on the basal plane (Tyson, 1971; Landgon, 1973; Hondoh, 2000).
- 80
6. Dislocation motion in ice is thought to be controlled in some way by proton disorder (Glen, 1968). Experimental work by Chan et al. (1965) on polycrystalline ice and Taubenberger et al. (1973) on single crystal ice both demonstrate that proton relaxation times increase with increasing  $P$ . This effect is expected to be quite small over the pressure range of our study, with a change in proton relaxation time of less than 5% for a pressure change of 20 MPa. In thermodynamic regions where proton-disorder control of basal dislocation glide is a likely rate-limiting mechanism, dislocation motion and therefore strain rate may decrease slightly with increasing pressure. Petrenko and
- 90

Whitworth (1999) suggest that the barrier to motion presented by the proton disorder mechanism should be much higher for reconstructed dislocations than for partials.

95  
7. Dislocation climb requires a supply of point defects. In the case of ice at under pressure, the concentration of self-interstitials is slightly higher (Hondoh et al., 1987; Hondoh, 2000) than at atmospheric pressure (2.9 ppm at  $P=20$  MPa vs 2.78 ppm at 0.1 MPa). In thermodynamic regions where self-interstitial driven dislocation climb is the rate-limiting process, we might expect a modest increase in recovery and strain rate with increasing  $P$ .

We note that the above effects can be expected to have conflicting impacts on both the strain rate and microstructural development of polycrystalline ice.

### 1.2. Review of Single Crystal Experiments

Studies of hydrostatic pressure effects on the dominant  $(0001)\langle 11\bar{2}0 \rangle$  basal slip system in single ice crystals have found two very different behaviors. Rigsby (1958) found no pressure effect on basal creep rate at constant homologous temperature  $T_h = T/T_m(P)$ , where  $T$  is the absolute temperature, and  $T_m$  is the melting temperature, which is a function of hydrostatic pressure. Cole (1996) found no pressure effect on the steady state creep rate at constant *absolute* temperature. These results, though somewhat contradictory, both emphasize that the pressure effect on the basal slip system, if it exists, is small within the  $P$  range relevant to ice on Earth.

### 1.3. Review of Polycrystal Experiments

Work to date on polycrystalline ice has shown a measurable effect on creep strain rates due to elevated hydrostatic pressure. Early testing was performed by Haefeli et al. (1968) who compared creep strain rates both at  
120 constant absolute and constant homologous temperatures at pressures of 0.1 and 32 MPa. In contrast to single crystal behavior, they found that elevated hydrostatic pressure increased the creep rate at a fixed absolute temperature, though conducting the test at the equivalent homologous temperature and atmospheric pressure increased it still more. No microstructural analysis of  
125 the creep-deformed specimens was reported and applied axial stresses were  $< 0.1\text{MPa}$ .

Jones and Chew (1983a) tested polycrystalline ice at a variety of pressures from 0.1 up to 50 MPa, an applied axial stress of 0.47 MPa and a constant absolute temperature of  $-9.6^\circ\text{C}$ . Significantly, they found that secondary creep rates slowed with increasing  $P$ , passed through a minimum at  
130  $\sim 15$  MPa hydrostatic pressure, and then increased rapidly up to the maximum test condition of  $P=60$  MPa. This result implies that the activation volume for creep either *changes sign* or *changes from zero to a large negative value* at  $\sim 15$  MPa. The creep rate increase was attributed to the proximity  
135 of the system to the pressure melting point and therefore enhanced sliding along wetted grain boundaries. No microstructural analysis of the creep-deformed specimens was reported.

Durham et al. (1983) performed constant strain rate tests on polycrystalline ice specimens with the goal of characterizing the rheology of water  
140 ice in the outer solar system. A high pressure in this context is  $\sim 300$  MPa,

whereas a high pressure for natural ice on earth is  $\sim 30$  MPa. The temperature and pressure ranges covered in Durham et al. (1983) are generally much more extreme than those on Earth, though their data and the data of Jones and Chew (1983a) do overlap near  $P=50$  MPa. In the region of overlap, the  
145 two groups have found roughly similar magnitudes but opposite signs for the activation volume  $V^*$ . Near  $P=50$  MPa, Jones and Chew (1983a) found that creep rate increased with pressure (i.e.  $V^* < 0$ ). Durham et al. (1983) found that between 0.1 and 50 MPa pressure, increased pressure led to a slight hardening of the ice (i.e.  $V^* > 0$ ). The discrepancy between these  
150 results may be related to the pre-test microfracturing issues detailed in the Discussion section of Durham et al. (1983).

Tests performed at confining pressures up to 31.5 MPa by Mizuno (1992) found that the effects of  $P$  on secondary creep rate were limited to temperatures above a critical temperature of  $-6^\circ\text{C}$ . Applied axial stresses were  
155 high and ranged from 1 to 3 MPa. Analysis of optical thin sections taken from the creep-deformed specimens showed that, for specimens deformed above this critical temperature, rapid and extensive recrystallization and grain growth rendered the microstructure (in tertiary creep) independent of strain, while those deformed below this temperature featured microstructures  
160 which evolved more gradually with increasing strain. The resulting  $c$ -axis fabrics were girdle patterns centered on the compression direction; no fabric differences between specimens deformed at atmospheric and elevated hydrostatic pressures were reported.

#### 1.4. Motivation

165 The varied and often conflicting results discussed above underscore the experimental difficulties associated with confined creep testing. However, taking these results together with the list of possible  $P$  effects in Section 1.1, we can surmise that

1. The observed changes of creep rate and activation volume with  $P$  in polycrystalline ice is not due to a fundamental change in the basal slip system dynamics.
2. The enhanced creep rates are derived from the presence of grain boundaries (GB) or stress heterogeneities (or both) found in polycrystals, and not in single crystals.
- 175 3. Microstructural analysis of the creep-deformed specimens, which was largely lacking in earlier work, may aid in separating the effects of temperature and hydrostatic pressure on creep deformation of ice.

In this paper we seek to (1) document the microstructural and mechanical differences between specimens deformed at  $P=0.1$  and  $P=20$  MPa, (2) 180 discuss possible mechanisms for the observed microstructural differences and (3) argue that the observed effects of hydrostatic pressure on the creep of polycrystalline ice are not solely due to changes in the homologous temperature, but instead reflect pressure-induced changes in dislocation and grain boundary dynamics.

185 We offer two possible hypotheses to explain the findings in the existing literature and the new results presented in this paper. Hypothesis (1): Increased strain rates are caused by the pressure-induced constriction and

reconstruction of dissociated basal dislocations at  $P \geq$  a critical pressure  $P_c$ , Hypothesis (2): Basal dislocation glide, controlled by proton disorder effects, is the rate controlling process at low pressures while climb, driven by higher equilibrium self-interstitial concentrations, becomes rate controlling at high pressures.

Both hypotheses seek to explain the shift from positive to negative  $V^*$  with increasing pressure observed by Jones and Chew (1983a) and our own microstructural observations of creep-deformed specimens. At this point, the results of this on-going work are not definitive, but the above hypotheses are explored in an effort to stimulate continued interest in this important topic.

## 2. Methods

### 2.1. Test Specimens

We generated test specimens of polycrystalline ice with random crystal orientations using the methods of Cole (1979). The cylindrical ice specimens were 34 mm diameter by 86 mm tall with 25 mm tall corrugated phenolic endcaps frozen directly to the specimen ends during the fabrication process. The endcaps ensure proper parallelism of the specimen ends and correct axial alignment of the specimen within the uniaxial creep testing system. Specimens were stored at  $-30^\circ\text{C}$  for storage both before and after mechanical testing to minimize microstructural changes while in storage.

## 2.2. Confined Creep Testing

210 The uniaxial creep testing system applies a constant load to the test specimens via modular lead weights and machined steel plates at the interface between ice and lead to provide a smooth and axially true loading surface. The weights are constrained to move vertically by polished steel guide rails and linear bearings. Two specimens can be tested simultane-  
215 ously by building a stack from the bottom up, shown in Figure 1.

The load applied to the lower specimen is then the sum of the upper and lower weights, while the upper specimen experiences the load from the upper weights only. The modular weights allowed adjustment of the applied stresses from 0.1 to 0.63 MPa; higher stresses are not possible given the  
220 limited volume within the pressure vessel.

Creep displacement was measured (2.5 microstrain resolution) separately on each specimen by vented,  $\pm 6$ mm range LVDTs (Macrosensors, Pennsauken, NJ) mounted rigidly to the specimen endcaps. Specimen temperature was monitored using a thermistor string (Thermometrics, Northridge, CA) ac-  
225 curate to  $\pm 0.01^\circ\text{C}$ . System hydrostatic pressure was measured (690 Pa resolution) by a pressure transducer (Dynisco, Franklin, MA) and all voltages and temperatures were recorded at 60 sec intervals on a dedicated data acquisition computer.

Once set up, the creep testing system is placed into the pressure vessel,  
230 the vessel filled with Dow Corning 550 silicone oil, sealed, and pressurized using a hand pump. Pressurization/depressurization rates are limited to 150 kPa  $\text{min}^{-1}$  to minimize adiabatic heating/cooling (typically less than  $1^\circ\text{C}$ ) of the specimen. Pressure control (stable to within 1%) is achieved via a 3.8 L

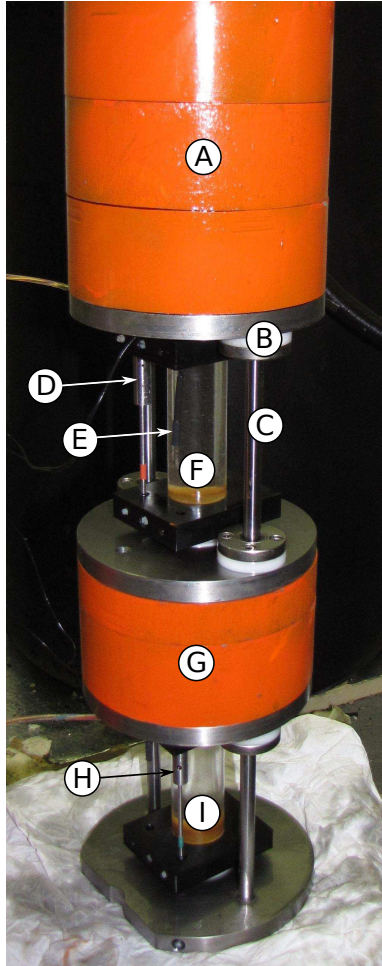


Figure 1: Photograph of uniaxial creep testing system ready for installation into the pressure vessel; double specimen setup is shown here. A - upper weight stack, B - linear bearing, C - guide rail, D - upper specimen LVDT, E - thermistor, F - upper ice specimen, G - lower weight stack, H - lower specimen LVDT, I - lower ice specimen.

hydraulic accumulator precharged to 15 MPa with N<sub>2</sub> gas, which supplies a  
235 sufficient volume of makeup oil for multi-month tests and minimizes pressure  
variations associated with temperature changes within the cold room.

The pressure vessel is then placed into a 200 L barrel of ethylene gly-  
col which is maintained at a steady temperature ( $\pm 0.5^\circ\text{C}$ ) by an Endocal  
(Thermo-Neslab, Newington, NH) RTE-4 refrigerated circulator. The ther-  
240 mal mass of the pressure vessel itself typically limits specimen temperature  
variations to  $\pm 0.1^\circ\text{C}$ . The final testing conditions (i.e. steady  $T$  and  $P$ ) are  
generally achieved within 4–6 h of first applying load to the specimens.

### *2.3. Specimen Microstructure Imaging*

Specimen-scale images of the specimen microstructure for grain size and  
245 shape were recorded using thin sections digitally photographed in transmit-  
ted light between crossed polarizers. The resulting images (typical resolu-  
tion  $17\ \mu\text{m}\ \text{pixel}^{-1}$ ) were analyzed using the freely available FIJI (Schindelin  
et al., 2012) image processing software. Grain sizes were determined for each  
grain by calculating the circular equivalent diameter, and we quantified the  
250 grain shapes by measuring circularity and solidity (Olson, 2011).

Smaller scale images were obtained on uncoated 1 cm by 3 cm specimens  
via SEM micrographs recorded on a FEI (FEI Inc., Hillsboro, OR) XL-30  
environmental scanning electron microscope equipped with a Gatan (Gatan  
Inc., Pleasanton, CA) C1002 cryostage. Images were typically recorded un-  
255 der 0.2 Pa of N<sub>2</sub> gas, with a cryostage temperature of  $-160^\circ\text{C}$ , using a 15 kV  
accelerating voltage and a large field gaseous secondary electron detector.  
Both the low temperature and slight N<sub>2</sub> gas pressure act to reduce speci-

men sublimation as discussed in Weikusat et al. (2011), thus preserving the specimen surface for several hours.

260 *2.4. Electron Backscatter Diffraction Mapping*

Electron Backscatter Diffraction (EBSD) determines the full  $a$  and  $c$  axis crystallographic orientation of ice grains and subgrains with an angular resolution  $< 1^\circ$  and a spatial resolution down to  $0.5\mu\text{m}$ . The electron beam of the SEM is used as the source and the resulting backscattered diffraction  
265 pattern (EBSP) is recorded on a phosphor screen, imaged by a video camera. We used an Oxford-HKL Technology EBSD system to automate the beam scanning, stage motion, diffraction pattern recording and analysis, as has been done in several earlier studies (see Iliescu et al. (2004) and Obbard et al. (2006)).

270 The diffraction itself takes place in a few nm closest to the specimen surface, so specimen surface preparation and maintenance is critical. We microtomed the analysis surface and allowed further smoothing via sublimation in a closed container at  $-25^\circ\text{C}$  for 6-12 h prior to analysis. However, a delay of more than 48 h under these sublimation conditions caused suffi-  
275 cient surface roughening to negatively affect the EBSD analysis. This procedure was followed for all specimens, so we cannot say that microstructural changes did not occur between removing the specimen from the confined creep apparatus and time of analysis in the SEM.

Ice grains are quite large ( $\sim 1\text{mm}$  or larger) compared to many other ma-  
280 terials, requiring the use of low magnifications (typically 40X) and stitching together contiguous EBSD maps to fully cover the  $3\text{ cm}^2$  area of the SEM

specimens. Large scale EBSD mapping was performed using an electron beam current of 20nA, enabling the collection of 3 orientation data points per second with a  $\sim 75\%$  successful EBSP indexing rate. Typically an 85  
285 or 100  $\mu\text{m}$  step size was used to generate large scale maps of useful resolution while still covering specimen area at a sufficient rate to ensure good surface quality throughout the analysis; approximately 1.25 h was required to analyze 3  $\text{cm}^2$  under these conditions.

The resulting orientation datasets were post-processed using both HKL  
290 Channel 5 software, as well as the open source MTEX toolbox (see Bachmann et al. (2011) and Bachmann et al. (2010)) to fill in non-indexed locations, determine grain boundaries and calculate average grain orientations and Schmid factors (Azuma, 1995; Trickett et al., 2000).

### 3. Results

295 A total of twelve specimens were tested under various conditions shown in Table 1. All were constant pressure tests except for S31MAY13, which was a variable pressure test.

#### 3.1. Mechanical Testing

The mechanical testing showed that both secondary and tertiary strain  
300 rates were enhanced at  $P=20$  MPa when compared to the same tests conducted at atmospheric pressure ( $P=0.1$  MPa). Strain rate minima occurred at similar strains (roughly 1%) for both  $P=20$  and 0.1 MPa which is interesting because the hydrostatic pressure induced a non-trivial shortening of the

Table 1: Listing of specimens and mechanical testing conditions. The date in the specimen designation indicates the date of fabrication. Temperature  $T$  is shown  $\pm$  one standard deviation. (a) S27FEB13 and S01MAR13 were tested together in the double specimen setup. (b) S29MAR13 and S27MAR13 were tested together in the double specimen setup. (c) Variable pressure test conducted in secondary creep.

Specimen	$P$ (MPa)	$\sigma$ (MPa)	$T$ ( $^{\circ}\text{C}$ )	$T_h$	$\dot{\epsilon}_{\min}$ ( $\text{s}^{-1}$ )	Final $\epsilon$	Duration (h)
S22OCT12	20.0	0.63	$-5.06 \pm 0.07$	98.68%	$1.7 \times 10^{-8}$	8.86%	622
S20NOV12	20.0	0.63	$-5.04 \pm 0.09$	98.69%	$1.8 \times 10^{-8}$	8.83%	554
S11DEC12	0.1	0.63	$-4.94 \pm 0.04$	98.19%	$1.4 \times 10^{-8}$	9.23%	760
S11JAN13	0.1	0.63	$-3.60 \pm 0.10$	98.68%	$3.5 \times 10^{-8}$	9.41%	388
S01FEB13	0.1	0.63	$-2.48 \pm 0.06$	99.09%	$1.0 \times 10^{-7}$	8.81%	304
S27FEB13 <sup>a</sup>	20.0	0.33	$-4.74 \pm 0.32$	98.80%	$5.0 \times 10^{-9}$	0.96%	335
S01MAR13 <sup>a</sup>	20.0	0.50	$-4.74 \pm 0.32$	98.80%	$2.4 \times 10^{-8}$	6.14%	335
S29MAR13 <sup>b</sup>	20.0	0.33	$-9.67 \pm 0.07$	96.98%	$1.5 \times 10^{-9}$	1.31%	1390
S27MAR13 <sup>b</sup>	20.0	0.50	$-9.67 \pm 0.07$	96.98%	$4.4 \times 10^{-9}$	6.18%	1390
S31MAY13 <sup>c</sup>	0.1 to 15	0.50	$-4.80 \pm 0.47$	variable	$1.2 \times 10^{-8}$	1.23%	180

specimen (estimated at 0.1%) that apparently contributed to the transition  
305 from primary to secondary creep.

Our constant pressure test results plotted in Figure 2 show that for equal  
absolute temperatures, a specimen deformed at  $P=20$  MPa (e.g. S20NOV12)  
deforms faster than one deformed at  $P=0.1$  MPa (S11DEC12). However, a  
specimen deformed at atmospheric pressure and at the equivalent homolo-  
310 gous temperature (S11JAN12) deforms faster than the pressurized specimen  
(S20NOV12). These results are consistent with the findings (see Section 1.3)  
of Haefeli et al. (1968).

In testing any polycrystalline specimen, a certain amount of specimen-  
to-specimen variability is inevitable due to random differences in grain sizes,  
315 crystallographic orientations and initial dislocation densities that occur dur-  
ing specimen fabrication. Because of the long deformation times involved  
in creep testing, we have only two specimens, S22OCT12 and S20NOV12,  
that were deformed under the same  $P$ ,  $T$ , and  $\sigma$  conditions, resulting in a  
difference of  $1 \times 10^{-9} \text{ s}^{-1}$  in the minimum strain rate. This value is in rea-  
320 sonable agreement with the  $3 \times 10^{-9} \text{ s}^{-1}$  specimen-to-specimen variability  
observed between six specimens deformed at atmospheric pressure in Jones  
and Chew (1983a). Assuming that  $3 \times 10^{-9} \text{ s}^{-1}$  is a reasonable estimate,  
the differences in strain rate attributed to pressure and temperature effects  
in our study are roughly 6-10 times larger than the specimen-to-specimen  
325 variability, and thus are readily distinguishable from it. Ideally, numerous  
repeat creep experiments would be run to better characterize this variability,  
but practical constraints on testing time prevent this.

The variable pressure test (S31MAY13) was designed to reproduce that

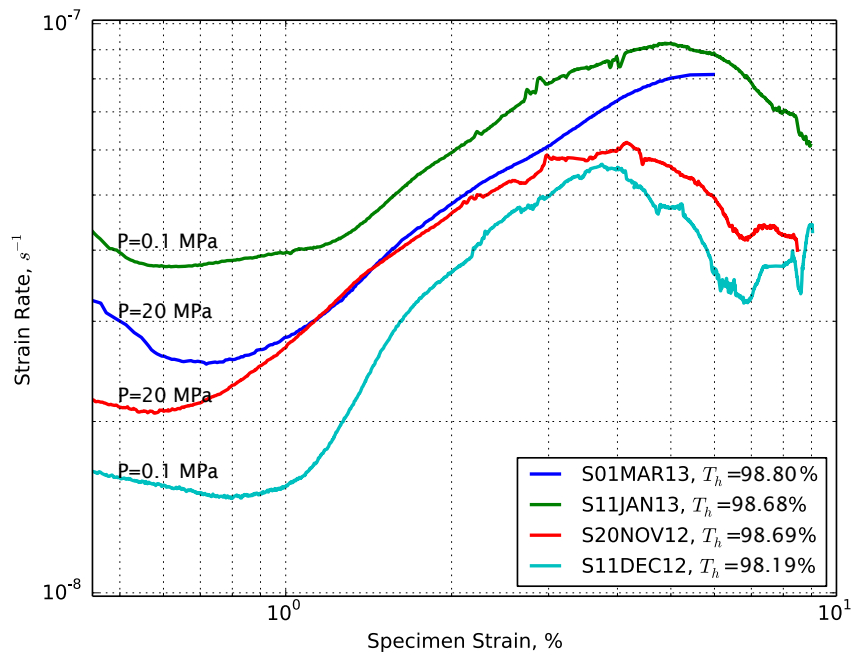


Figure 2: Strain rates vs. strain for specimens deformed at the same absolute temperature (S20NOV12 and S11DEC12) and for specimens deformed at the same homologous temperature of  $T_h=98.7\%$  (S20NOV12 and S11JAN13). Specimen S01MAR13 was deformed with  $\sigma=0.50$  MPa, while all other specimens were deformed with  $\sigma=0.63$  MPa.

Table 2: Variable pressure test schedule for S31MAY13 with  $\sigma = 0.50$  MPa. At least 24 h elapsed between each pressure change to allow stabilization of temperature and strain rate. Temperature variations of  $0.5^\circ\text{C}$  were typical.

$P$ (MPa)	$T$ ( $^\circ\text{C}$ )	$T_h$ (%)	$\epsilon$	$\dot{\epsilon}$ ( $\text{s}^{-1}$ )
0.1	-5.05	98.17	0.33%	$1.6 \times 10^{-8}$
5.0	-4.95	98.30	0.53%	$1.7 \times 10^{-8}$
10.0	-4.88	98.44	0.71%	$1.4 \times 10^{-8}$
15.0	-4.85	98.57	0.85%	$1.4 \times 10^{-8}$
0.1	-5.10	98.17	1.23%	$1.3 \times 10^{-8}$

of Jones and Chew (1983a), but at a higher homologous temperature. We prepared the specimen by first deforming it at  $P=0.1$  MPa until it reached secondary creep, and then increased  $P$  in 5 MPa steps and recording strain rate 24 h after the pressure change. The resulting strain rates are shown in Table 2, indicating little change in strain rate with increasing pressure from 0.1 to 15 MPa. Temperature control for this experiment was not as good as that of the constant pressure tests due to the varying  $P$  and mechanical problems with the cold room.

### 3.2. Grain Size and Shape

The median grain diameter  $\bar{d}$  for  $P=20$  MPa specimens increased slightly in the early stages of deformation ( $\epsilon < 1\%$ ), as expected from the work of Azuma and Higashi (1983). The grain size distribution was narrow, approximately log-normal and mainly consisted of equiaxed grains.

At strains approaching 6% we found a rapid decrease in  $\bar{d}$ . The grain size distribution was approximately log-normal and very wide: a few large irregularly shaped grains were surrounded by smaller, approximately equiaxed grains.

At our highest strains, approaching 9%, the grains were large, heavily

subgrained, and amœboid in shape. The grain size distribution was narrower than that observed at  $\epsilon = 6\%$ , but still much wider than the initial, unstressed state. Observations in the SEM shows significant amounts of grain growth directed along subgrain boundaries (sGB).  
350

Specimens deformed to strains around 9% at  $P=0.1$  MPa also demonstrated some amœboid grains and, when observed in the SEM, less directed grain growth.  $\bar{d}$  was larger than that of specimens deformed to similar strains at  $P=20$  MPa, as shown in Table 3 and Figure 3.

### 355 3.3. Subgrain Boundaries

We observed the formation of subgrain boundaries in all specimens using sublimation-etched ice techniques similar to those discussed in Hamann et al. (2007) and Weikusat et al. (2011), and by performing a kernel averaged misorientation (KAM) analysis (Brewer et al., 2009) on one of our few high resolution EBSD datasets, shown in Figure 4. The spatial variability of sGB density (estimated by sublimation etching techniques) within a given specimen was significant, no doubt due to the well known inhomogeneity of the stress and strain fields within polycrystalline ice (Grennerat et al., 2012).  
360

Individual sGBs can be observed in high resolution ( $\sim 10 \mu\text{m}$  step size) KAM analyses and this technique can correctly identify high angle grain boundaries where contrast analysis of sublimation grooves fails (see Label d in Figure 4). Unfortunately, routine analysis of ice at this resolution is only possible on very small areas (about  $4 \text{ mm}^2$ ) because of the sublimation rate of the ice surface during analysis in the SEM. This is especially problematic  
370

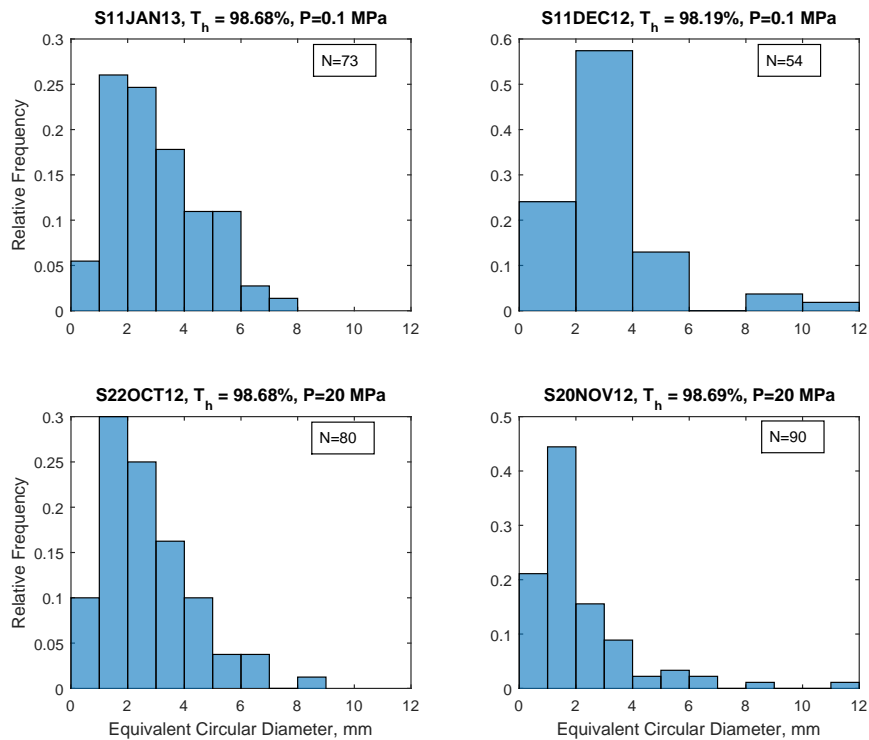


Figure 3: Grain size distributions for the four most strained specimens, as determined by analysis of cross-polarized thin section images.  $N$  indicates the number of grains used in each analysis.

Table 3: Grain size and shape data for creep specimens. A value of  $\sim 10$  or more grains across the specimen diameter ensures that the specimen is truly polycrystalline for the purposes of creep testing (Jones and Chew, 1983b).

Specimen	$P$ (MPa)	$\sigma$ (MPa)	T (°C)	$T_h$	Final $\epsilon$	$d$ mm	Average Solidity	Average Circularity	Grains across spec. diam
Unstrained	0.1	-	-	-	0%	$2.30 \pm 0.025$	$0.946 \pm 0.001$	$0.805 \pm 0.001$	14.75
S01FEB13	0.1	0.63	-2.48	99.09%	8.81%	$3.29 \pm 0.035$	$0.891 \pm 0.001$	$0.639 \pm 0.001$	10.3
S20NOV12	20.0	0.63	-5.04	98.69%	8.83%	$1.52 \pm 0.026$	$0.823 \pm 0.001$	$0.585 \pm 0.001$	11.9
S22OCT12	20.0	0.63	-5.06	98.68%	8.86%	$2.52 \pm 0.028$	$0.812 \pm 0.001$	$0.544 \pm 0.001$	10.9
S11JAN13	0.1	0.63	-3.60	98.68%	9.41%	$2.70 \pm 0.029$	$0.852 \pm 0.001$	$0.608 \pm 0.001$	9.4
S11DEC12	0.1	0.63	-4.94	98.19%	9.23%	$2.77 \pm 0.033$	$0.873 \pm 0.001$	$0.666 \pm 0.001$	9.6

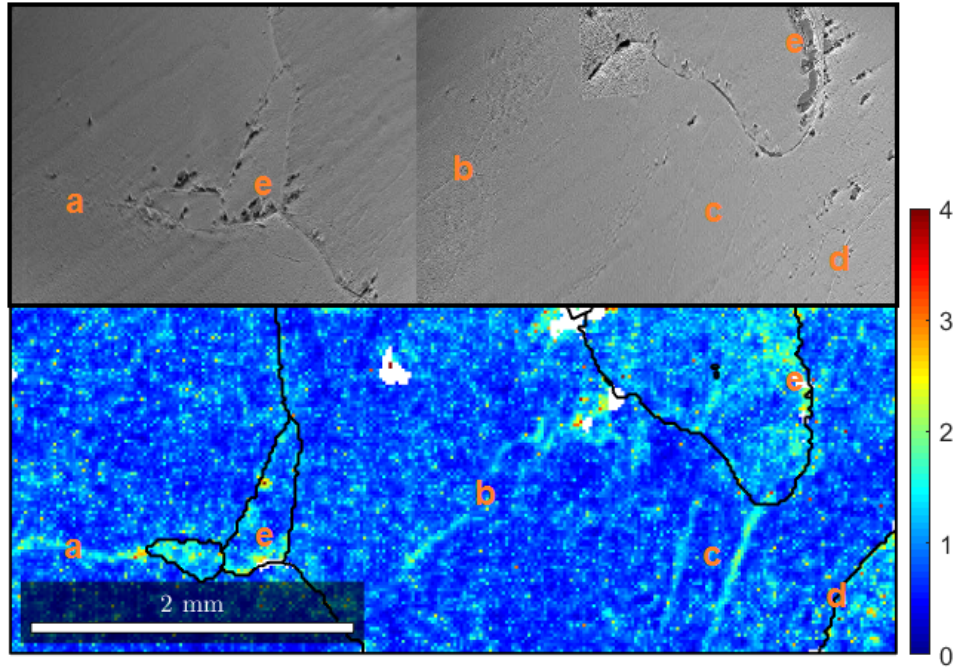


Figure 4: Micrographs and KAM analysis of S11DEC12. Upper half shows secondary electron micrographs of the specimen surface, showing surface topography. Lower half shows a map of KAM values (in units of degrees misorientation) derived from a high resolution EBSD map of the same specimen. Labels a, b, and c show the locations of sGBs that are visible in the micrograph and detectable in the misorientation analysis. Label d shows a high angle GB that is indistinguishable from sGBs on the basis of micrograph contrast alone. Label e shows locations where surface imperfections lead to higher values of misorientation without the presence of sGBs.

given the large grain size of ice and spatial variability of subgrain boundary densities within a single specimen.

### 3.4. Fabric

Ice fabrics were generally similar between  $P=0.1$  and  $P=20$  MPa specimens, as shown in Figure 5c, Figure 6c and Figure 7d. We were limited in the number of grains available for analysis in the SEM due to the large grain size of ice.

The most of the EBSD maps shown use a Schmid factor (Trickett et al., 2000) coloration to demonstrate the relative magnitude of the resolved shear stress on the  $(0001)\langle 11\bar{2}0 \rangle$  basal slip system of a given crystal orientation imposed by the axial load  $\sigma$ . The Schmid factor can range from 0.5 for a “easy-glide” orientation (typically shown in red) to 0 for a “hard-glide” orientation with the  $c$ -axis parallel to  $\sigma$  (typically shown in blue).

The Schmid factor maps indicate that, despite the overall similarity of the fabrics between  $P=20$  MPa and  $P=0.1$  MPa specimens, the spatial distribution of the grains making up that fabric can be different. Though our EBSD data are too limited to draw general conclusions, we have observed large “hard-glide” grains surrounded by clusters of smaller “easy-glide” grains which may serve a mechanism to decouple the hard grains from each other and promote bulk strain primarily via the “easy-glide” clusters or bands Passchier and Trouw (2005).

#### 4. Discussion

The results of our mechanical testing are consistent with the literature:

1. At the same  $T$ , secondary and tertiary strain rates are larger at  $P=20$  MPa compared to  $P=0.1$  MPa (i.e. comparing S20NOV12 with S11DEC12).

The pressure-induced increase is not as large as that obtained by deformation at the same  $T_h$  (Haefeli et al., 1968) (i.e. comparing S20NOV12 with S11JAN13). The fact that specimens deformed at equal homologous temperatures *do not* have equal strain rates is an important clue that processes other than the pressure melting effect are contributing to the observed changes in strain rate.

# figures / S22OCT12

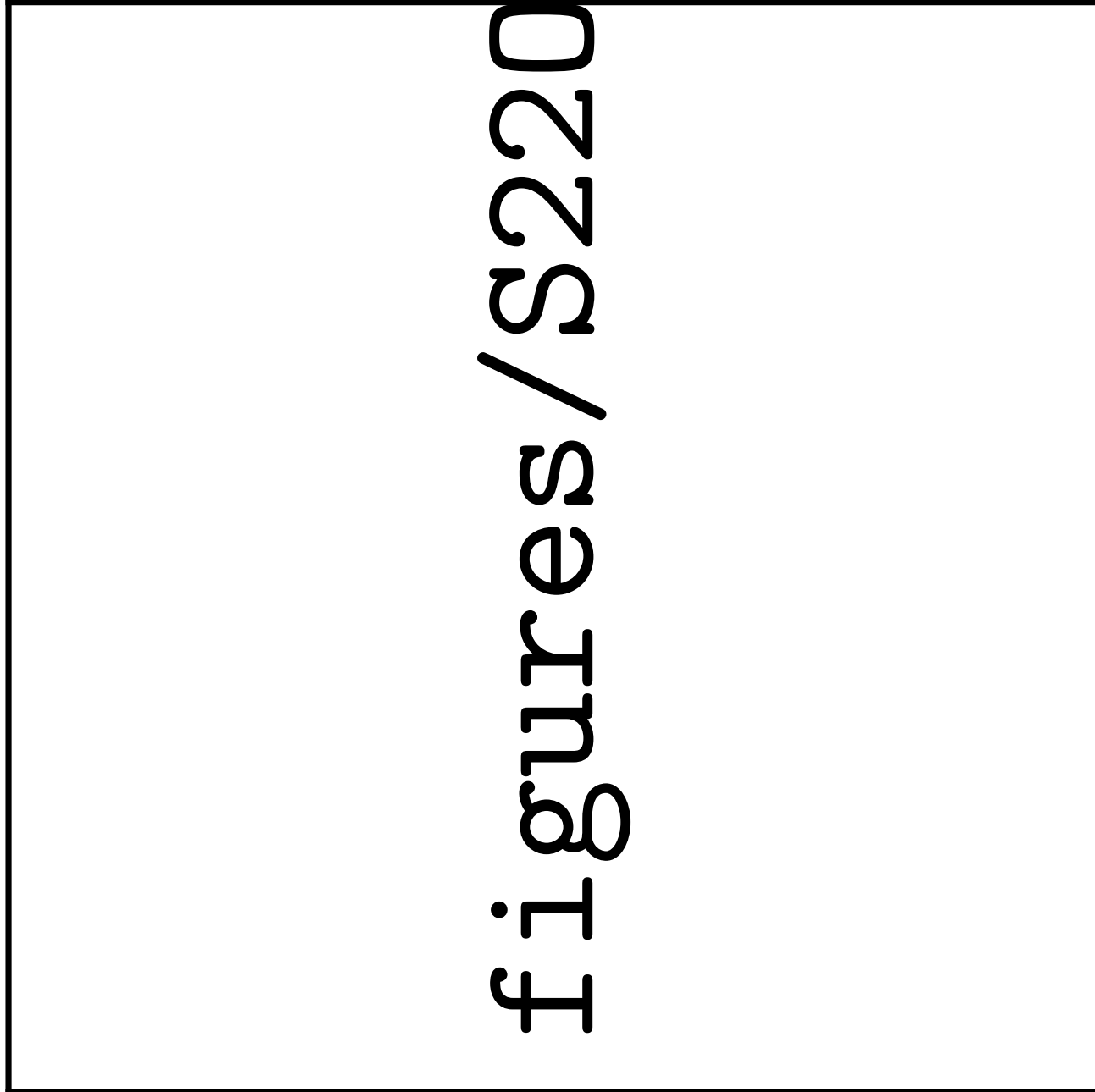


Figure 5: (a) EBSD map of specimen S22OCT12 strained 8.86% at  $P=20$  MPa and  $T = -5^{\circ}C$ , Schmid factor coloration. (b) Schmid factor histogram for all data points. (c)  $c$ -axis pole figure, one point per grain. (d) Detail of grain boundary migration directed along subgrain boundaries and subsequent rotation recrystallization. (e) Detail of extensive subgrain development, even within “easy” glide grains. (f) Detail of directed grain boundary migration along subgrain boundaries.

# figures / S11DEC12

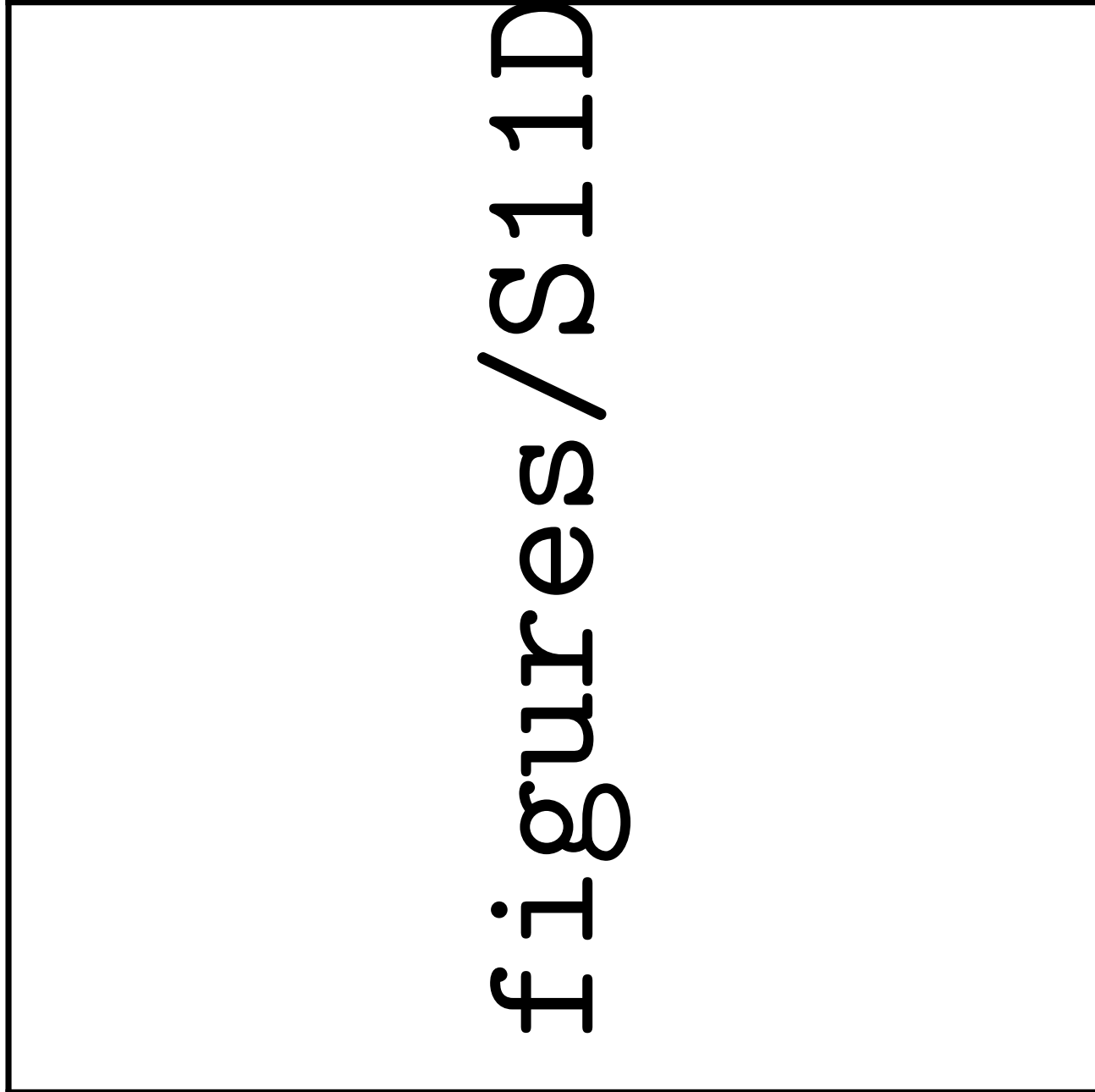


Figure 6: (a) EBSD map of specimen S11DEC12 strained 9.23% at  $P=0.1$  MPa and  $T = -5^{\circ}C$ , Schmid factor coloration. (b) Schmid factor histogram. (c)  $c$ -axis pole figure, one point per grain. (d1) Detail of grain-subgrain interaction. (d2) High resolution EBSD map showing  $\pm 3^{\circ}$  intragranular misorientations.

# figures / S01MAR13

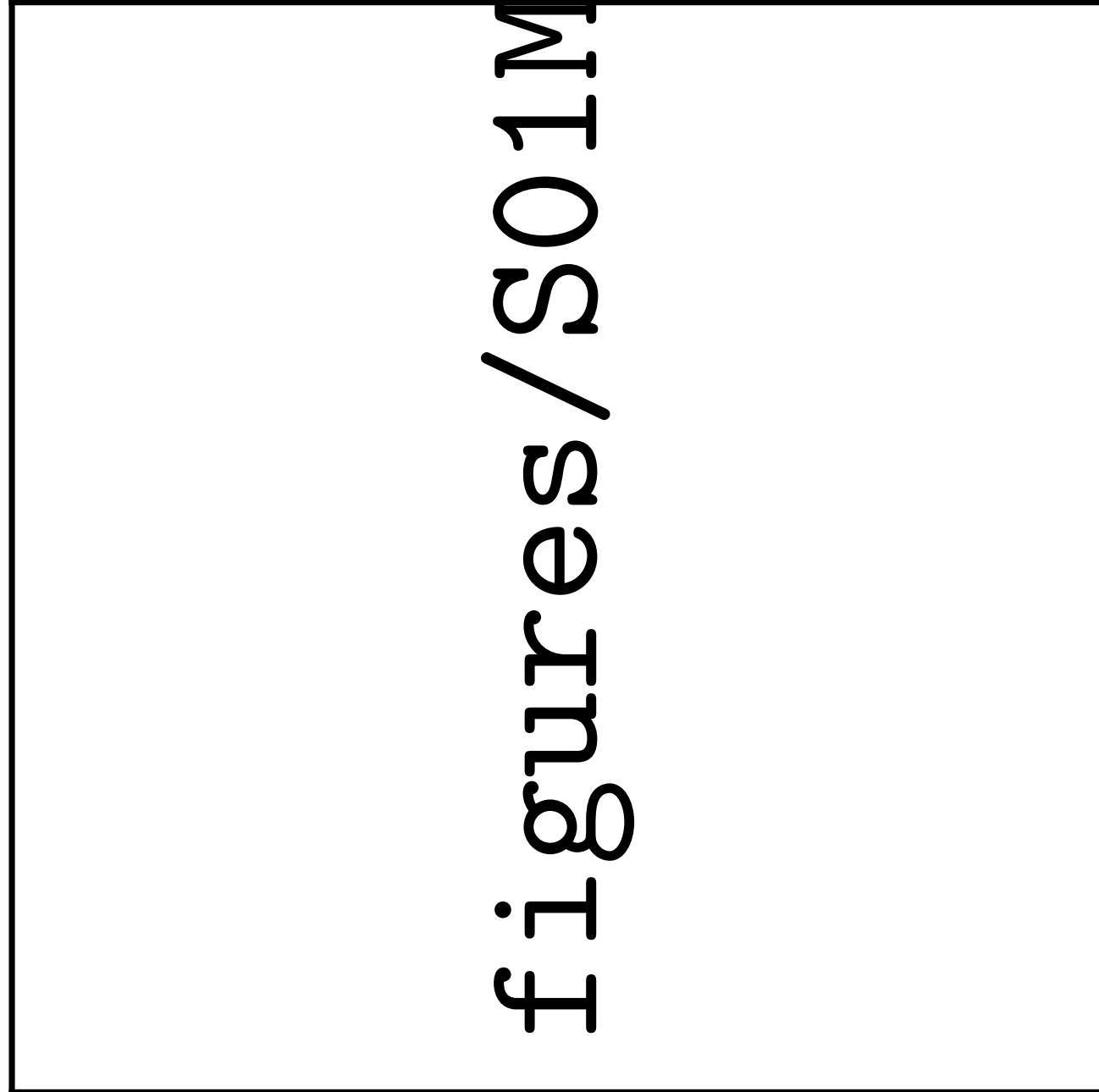


Figure 7: (a) EBSD map of specimen S01MAR13 strained 6.14% at  $P=20$  MPa and  $T = -5^{\circ}C$ , Inverse Pole Figure coloration shown in (b). (c) Schmid factor histogram. (d)  $c$ -axis pole figure, one point per grain. (e) Detail of dissected grain. (f) Detail of grain boundary migration and bulging.

2. The enhancement factor  $\dot{\epsilon}_{\text{tertiary}}/\dot{\epsilon}_{\text{min}} \approx 3$  for all  $P$  tested (Treverrow et al., 2012).
3. The minimum strain rate  $\dot{\epsilon}_{\text{min}}$  occurs around 1% for all  $P$  tested.
- 405 4. Strain rates for  $P \leq 15$  MPa were essentially unchanged by the application of confining pressure in the variable pressure testing on S31MAY13. It is significant that this result was observed at  $98.17\% \leq T_h \leq 98.57\%$ , nearly 2% higher than the variable pressure test conditions of Jones and Chew (1983a) which showed a similar lack of response for  $P \leq 15$  MPa.

The pressure melting effect of ice complicates the interpretation of the mechanical results as it is difficult to separate the effects of changing the homologous temperature from those associated with pressure effects on the material properties or dislocation dynamics of ice. Jones and Chew (1983a) discuss a liquid-enhanced grain boundary sliding hypothesis to describe their results and is consistent with  $V^* < 0$  at  $P > 15$  MPa because the liquid state of water occupies less volume than the solid. If their hypothesis is true, and some critical value of  $T_h$  near 96.3% is the minimum required to activate liquid-enhanced grain boundary sliding processes, then our variable pressure test should have shown increasing strain rate with *any* increase in pressure over atmospheric. However, the null result of our variable pressure test implies  $V^* \approx 0$  for  $P \leq 15$  MPa and we must therefore consider other mechanisms consistent with a negative  $V^*$  for  $P > 15$ MPa.

#### 4.1. Pressure-enhanced recovery in ice

425 Recovery is typically associated with the softening of dislocation-hardened crystals. Dislocation mobility is an essential part of recovery as it allows a dislocation the possibility of moving around obstacles, enabling further plastic deformation and lowering the stored strain energy (Lothe and Hirth, 1967).

430 The extreme plastic anisotropy of ice derives from the dissociation of dislocations on the basal plane (Fukuda et al., 1987); extended dislocations glide only on the basal plane and are unable to move unless constricted or fully recombined (Hondoh, 2000; Argon and Moffatt, 1981; Sherby and Burke, 1968). Thus recovery in ice is generally difficult and strain energy is  
435 readily concentrated such that recrystallization becomes a viable means of reducing this energy (Duval et al., 2012; Ueki et al., 1987).

By making some simplifying assumptions regarding the variation of the energy of a stacking fault as a function of lattice dilatation, Fontaine and Haasen (1969) calculated the width of a dissociated dislocation and de-  
440 termined that there should exist a *critical hydrostatic pressure*  $P_c$  at which point it is no longer energetically favorable for the dislocation to split. Their expression for dissociated width  $w$  is

$$w = \frac{Gb^2(1 + \kappa_0^2/4)}{2\pi(1 - \nu)(\gamma_0 + \kappa_0 bP/2)} \quad (2)$$

where  $b$  is the magnitude of the Burger's vector of the perfect dislocation,  $\gamma_0$  is the stacking fault energy at  $P=0.1$  MPa,  $\kappa_0$  is the lattice dilatation  
445 associated with a stacking fault at  $P=0.1$  MPa, and  $\nu$  is Poisson's ratio.

Fontaine and Haasen estimated that the critical pressure to begin observing pressure-induced constriction effects on  $w$  occurred when

$$\kappa_0 b P_c / 2 \approx F \gamma_0. \quad (3)$$

where they chose  $F=0.1$ . In other words, pressure effects on  $w$  should begin when the  $PV$  energy of the stacking fault dilatated lattice at pressure  $P_c$  reaches 10% of the stacking fault energy of the material. Fontaine and Haasen explain their choice of this 10% constriction threshold to merely establish the order of magnitude of  $P_c$ . The critical pressures for the various stacking faults in ice as a function of  $\kappa_0$  are shown in Fig. 8 where we plot curves both for Fontaine and Haasen’s 10% threshold and for the “100% threshold” where  $F=1$  where pressure effects on  $w$  would be almost certain. We therefore regard the the 10% and 100% thresholds as lower and upper bounds for the range of  $P_c$  for the various stacking fault energies.

Values of  $\kappa_0$  are not known for the various stacking faults in ice, but they are likely small given the low stacking fault energies observed in ice (Hondoh, 2013). The critical pressures for the lowest energy ( $0.3 \text{ mJ m}^{-2}$ ) stacking fault could be consistent with the change in sign of  $V^*$  around  $P=15 \text{ MPa}$  observed by Jones and Chew (1983a) if  $0.006 < \kappa_0 < 0.01$  and Fontaine and Haasen’s 10% threshold is correct. For the 100% threshold, the lattice dilatation would need to be an order of magnitude larger ( $0.06 < \kappa_0 < 0.1$ ) to explain the same change in sign.

The initial reduction in creep rate with pressure (i.e.  $V^* > 0$ ) may be caused by the usual diffusion-retarding effects of pressure (Butcher and

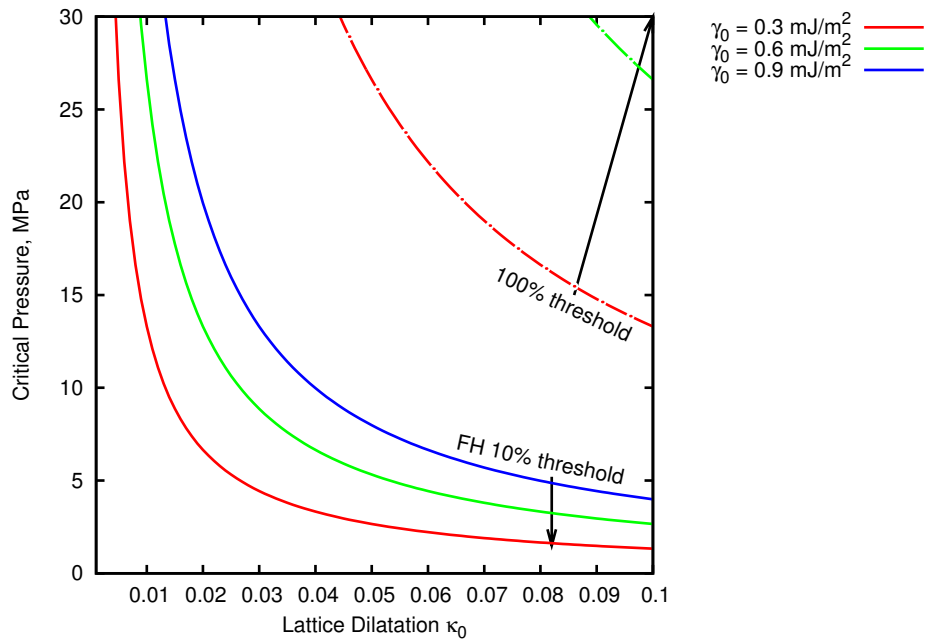


Figure 8: Critical pressure  $P_c$  vs lattice dilatation  $\kappa_0$  for three possible stacking fault energies in ice. Solid curves show  $P_c$  for Fontaine and Hassen's 10% pressure effect threshold, while upper dot-dash curves show the full 100% threshold. The lattice dilatation due to a stacking fault is not known for ice, but is likely small. The change from positive to negative  $V^*$  observed by Jones and Chew (1983a) occurs between  $P=10$  to 15 MPa.

Ruoff, 1961; Hahn and Gleiter, 1979). However, we hypothesize (Hypothesis (1) in Section 1.4) that the subsequent increase in creep strain rate with  
470 pressure (i.e.  $V^* < 0$ ) beyond  $\sim 15$  MPa may be caused by the constriction of dissociated dislocations, thus enhancing dislocation mobility in ice. Louchet (2004) argues that climb velocity of basal dislocations is limited by the low concentration of jogs. Pressure-induced constriction would act to reduce the energy required for jog formation, thus increasing jog concentration and potentially shifting the rate limiting process from one associated  
475 with dislocation drag to one associated with climb.

An alternative hypothesis (Hypothesis 2 in Sec. 1.4) for increased creep strain rate at high pressure is the higher equilibrium concentration of self-interstitial defects available to fuel climb processes. However, this hypothesis  
480 faces two significant challenges:

1. The increase in equilibrium self-interstitial concentration for a pressure change of 20 MPa is very small, leading to a supersaturation of only 4% relative to the equilibrium concentration at atmospheric pressures (Hondoh, 2009); a temperature reduction of less than 0.2 C yields the  
485 same supersaturation.
2. Monotonic changes in self-interstitial concentration with pressure are insufficient to explain the change in sign of  $V^*$ . Some change in rate controlling mechanism must be identified.

One possible argument is that the rate controlling process at lower pressures is basal dislocation drag, perhaps controlled by proton-disorder effects  
490 (Taubenberger et al., 1973) such that increases in pressure also increase the

proton relaxation time, reducing dislocation velocity and yielding  $V^* > 0$ . If, at higher pressures, dislocation climb becomes the rate controlling process, then increases in pressure would increase self-interstitial concentration, enhancing rates of climb and yielding  $V^* < 0$ . However, such an argument  
495 does not provide a cause for the change of rate controlling mechanism unless we appeal to the dislocation constriction effects of Hypothesis 1.

#### 4.2. Fabric and Texture

Microstructurally, we observed an unexpected reduction in median grain  
500 size and less regular grain shapes for specimens deformed at  $P=20$  MPa compared to those tested at  $P=0.1$  MPa. The reduced median grain size and irregular grain shape seems to be the result of grain dissection (Jessell, 1987) caused by enhanced GB migration along subgrain boundaries. As the driving force for this GB migration is the reduction of interfacial energy, no  
505 particular orientation seems to be preferred for dissection as can be seen in Fig. 7. However, we note that higher-angle sGBs should have both a higher interfacial energy and lower velocity (Higashi and Sakai, 1961) suggesting that directed GB migration may be more likely along these boundaries. The directed grain growth process leads to a different grain size distribution  
510 between  $P=0.1$  and  $P=20$  MPa specimens, but the fabrics are largely the same: a circle girdle around  $40^\circ$  as expected from prior work by Jacka and Maccagnan (1984).

Grain shapes for strains nearing 10% tend to be more equi-axed for  $P=0.1$  MPa, but amoeboid at  $P=20$  MPa, consistent with the directed  
515 grain growth along subgrain boundaries. The prevalence of interlocked

amoeboid grains means that deformation by grain boundary sliding is less likely to contribute to the bulk strain of the specimen, though some local strain accommodation may be achieved through this method.

#### *4.3. Mechanical effects of enhanced recovery*

520 The climb of basal dislocations provides two deformation systems independent of the basal slip system to, in the framework of the “self consistent” method, providing a total of four slip systems, which is sufficient for crystal plasticity (Ashby and Duval, 1985). Enhancing the climb recovery via hydrostatic pressure would act to lower the stress concentrations caused by  
525 grain incompatibility during deformation and generally act to increase the creep rate by increasing the dislocation mobility (Barrett and Sherby, 1965).

Weertman (1965) analyzed this process by postulating that diffusion along a dislocation core is much faster than bulk diffusion in the case of perfect dislocations, and approaches the rate of bulk diffusion as the dissociated  
530 dislocation width  $w$  becomes large. As climb depends on the formation and diffusion of point defects, the climb rate of an extended dislocation should depend on  $w$ . In turn,  $w$  decreases with increasing hydrostatic pressure and, if the dislocation is part of an array within a subgrain boundary, with increasing misorientation angle of that boundary.

535 Continuing this line of thought, Weertman (1968) modified the Nabarro-Herring (NH) creep model for the presence of subgrains, using the subgrain size rather than the grain size to characterize the bulk diffusion distances required for NH creep. This is especially important in ice as the nominal *grain* sizes are too large to allow the NH creep to play any significant role in

540 the creep deformation of glacial ice (Duval et al., 1983). Using the subgrain size as the characteristic bulk diffusion distance and a  $G/\sigma$  subgrain size dependence, Weertman (1973) argues that subgrain-modified NH can result in a creep law with  $n = 3$  if the dislocations mainly exist evenly spaced within subgrain boundaries.

545 The purpose of this discussion is not to advocate a specific theoretical creep model, but instead to elaborate a plausible mechanism through which hydrostatic pressure, by changing the effective stacking fault energy, can have a direct impact on dislocation mobility and thus creep rate in polycrystalline ice. Similar arguments have been made for the dependence of 550 climb velocity (Argon and Moffatt, 1981) and creep rate (Mohamed and Langdon, 1974) on the stacking fault energy.

In this discussion we have focused mainly on recovery via dislocation climb, but cross-slip (Poirier, 1976; Landgon, 1973; Akimov et al., 1980) is another possible recovery mechanism in ice that could be enhanced by 555 application of hydrostatic pressure. Poirier (1976) presents a constitutive equation for high temperature creep which explicitly includes climb and cross slip, where the activation energy for climb  $Q_C$  is equal to that of self diffusion  $Q_D$  and the activation energy for cross slip  $Q_S$  is a function of both  $\sigma$  and  $\gamma_F$ . In ice, with its widely extended basal dislocations, it seems 560 appropriate to also consider a  $\sigma$  and  $\gamma_F$  dependence for the climb activation energy. In this case, the constitutive equation would look like

$$\dot{\epsilon} = \dot{\epsilon}_{0,C} \left(\frac{\sigma}{G}\right)^3 \exp\left(-\frac{Q_C(\sigma, \gamma_F)}{kT}\right) + \dot{\epsilon}_{0,S} \left(\frac{\sigma}{G}\right)^2 \exp\left(-\frac{Q_S(\sigma, \gamma_F)}{kT}\right) \quad (4)$$

where the effective stacking fault energy is related to the hydrostatic pressure.

## 5. Conclusions

565 Our confined creep testing results are consistent with those reported in earlier literature for both constant and variable pressure tests. We have found significant microstructural differences, including median grain size and grain morphology, between polycrystalline specimens deformed at  $P=0.1$  and  $P=20$  MPa. We conclude that these differences are caused by directed  
570 grain growth along subgrain boundaries in specimens deformed at higher pressure, leading to a smaller median grain size and a dissection microstructure (Jessell, 1987).

We presented two hypotheses regarding the impact of confining pressure on creep strain rate in polycrystalline ice. We feel that Hypothesis 1 better  
575 explains our observations and the observations of others for the following reasons:

1. The change in sign of  $V^*$  around 15 MPa observed by Jones and Chew (1983a) could be explained by the existence of a critical confining pressure at which dissociated dislocations find it energetically favorable to constrict and thereby become more mobile and enhance creep strain  
580 rates.
2. Comparison of the variable pressure tests conducted in this work and by Jones and Chew (1983a) suggest that increased creep strain rate at  $P \geq 20$  MPa is not simply a result of pressure melting effects. Both

585 tests showed a negligible strain rate change for  $0.1 < P < 15$  MPa,  
despite the fact that our variable pressure test was conducted at a  
significantly higher  $T_h$ . This supports the idea of a critical pressure  
for creep strain rate enhancement, and suggests that it is not strongly  
temperature dependent, contrary to the strong temperature depen-  
590 dence we would expect for a pressure melting phenomenon.

The notion that dissociated dislocations in ice  $I_h$  are sensitive to confin-  
ing pressures is central to our hypothesis, and that sensitivity depends on  
both the unknown magnitude of lattice dilatation induced by stacking faults  
in ice, and the threshold (i.e the 10% threshold of Fontaine and Haasen) at  
595 which confining pressure effects on dissociated dislocations become impor-  
tant. Very small values ( $\kappa_0 < 0.005$ ) of lattice dilatation and a large thresh-  
old would preclude pressure-induced constriction of partial dislocations, at  
least in the 0.1 to 20 MPa pressure regime accessible to our equipment.  
Molecular dynamics simulations of stacking fault behavior in ice at varying  
600 pressures may be a practical method to estimate these parameters.

*Acknowledgments.* This work was supported by NSF Award PLR 1022703,  
“Strain-Induced Fabric Development in Ice Under Hydrostatic Pressure”.  
The authors would like to acknowledge the efforts of two anonymous re-  
viewers whose commentary and feedback greatly improved the focus of this  
605 paper. We also extend our thanks to Professor T. Hondoh for helpful com-  
ments and discussion. The authors are also grateful to D. Punt, C. Donnelly  
and W. Burch of ERDC-CRREL for their invaluable assistance with data  
acquisition, mechanical and hydraulic systems in support of this work.

## References

- 610 Ahmad, S., Ohtomo, M., Whitworth, R., 1986. Observation of a dislocation source in ice by synchrotron radiation topography. *Nature* 319, 659–660.
- Akimov, G., Streltsov, V., Zaitsev, V., et al., 1980. Effect of high hydrostatic pressure on dislocation structure parameters of slip bands in NaCl crystals. *Physica Status Solidi (a)* 57, 439–447.
- 615 Aladag, E., Davis, L., Gordon, R., 1970. Cross-slip and the plastic deformation of NaCl single and polycrystals at high pressure. *Philosophical Magazine* 21, 469–478.
- Argon, A., Moffatt, W., 1981. Climb of extended edge dislocations. *Acta Metallurgica* 29, 293–299.
- 620 Ashby, M., Duval, P., 1985. The Creep of Polycrystalline Ice. *Cold Regions Science and Technology* 11, 285–300.
- Azuma, N., 1995. A flow law for anisotropic polycrystalline ice under uniaxial compressive deformation. *Cold Regions Science and Technology* 23, 137–147.
- 625 Azuma, N., Higashi, A., 1983. Effects of the hydrostatic pressure on the rate of grain growth in Antarctic polycrystalline ice. *The Journal of Physical Chemistry* 87, 4060–4064.
- Bachmann, F., Hielscher, R., Schaeben, H., 2010. Texture Analysis with MTEX—Free and Open Source Software Toolbox. *Solid State Phenomena*

630 160, 63–68. URL: <http://dx.doi.org/10.4028/www.scientific.net/SSP.160.63>, doi:10.4028/www.scientific.net/SSP.160.63.

Bachmann, F., Hielscher, R., Schaeben, H., 2011. Grain detection from 2D and 3D EBSD data - Specification of the MTEX algorithm. *Ultramicroscopy* 111, 1720–1733.

635 Barrett, C., Sherby, O., 1965. Influence of Stacking-Fault Energy on High-Temperature Creep of Pure Metals. *Transactions of the Metallurgical Society of AIME* 233, 1116.

Brewer, L.N., Field, D.P., Merriman, C.C., 2009. Mapping and assessing plastic deformation using ebsd, in: *Electron backscatter diffraction in materials science*. Springer, pp. 251–262.  
640

Butcher, B., Ruoff, A., 1961. Effect of Hydrostatic Pressure on the High-Temperature Steady-State Creep of Lead. *Journal of Applied Physics* 32, 2036–2038.

Chan, R., Davidson, D., Whalley, E., 1965. Effect of pressure on the dielectric properties of ice I. *Journal of Chemical Physics* 43, 2376–2383.  
645

Cole, D.M., 1979. Preparation of polycrystalline ice specimens for laboratory experiments. *Cold Regions Science and Technology* 1, 153–159.

Cole, D.M., 1996. Observations of pressure effects on the creep of ice single crystals. *Journal of Glaciology* 42, 169–175.

650 Durham, W., Heard, H., Kirby, S., 1983. Experimental deformation of

- polycrystalline h<sub>2</sub>o ice at high pressure and low temperature: Preliminary results. *Journal of Geophysical Research: Solid Earth* 88, B377–B392.
- Duval, P., Ashby, M., Anderman, I., 1983. Rate-controlling processes in the creep of polycrystalline ice. *The Journal of Physical Chemistry* 87, 4066–4074.
- Duval, P., Louchet, F., Weiss, J., Montagnat, M., 2012. On the role of long-range internal stresses on grain nucleation during dynamic discontinuous recrystallization. *Materials Science and Engineering A* 546, 207–211.
- Fontaine, G., Haasen, P., 1969. Hydrostatic pressure and plastic deformation of the alkali halides. *Physica Status Solidi (B)* 31, K67–K70.
- Frost, H., Ashby, M., 1982. *Deformation Mechanism Maps*. Pergamon, Oxford.
- Fukuda, A., Hondoh, T., Higashi, A., 1987. Dislocation mechanisms of plastic deformation of ice. *Journal de Physique Colloques* 48, 163–173.
- Gammon, P., Kiefte, H., Clouter, M., 1983. Elastic constants of ice samples by brillouin spectroscopy. *The Journal of Physical Chemistry* 87, 4025–4029.
- Glen, J., 1968. The effect of hydrogen disorder on dislocation movement and plastic deformation of ice. *Physics of Condensed Matter* 7, 43–51.
- Grennerat, F., Montagnat, M., Castelnau, O., Vacher, P., Moulinec, H., Suquet, P., Duval, P., 2012. Experimental characterization of the intragran-

ular strain field in columnar ice during transient creep. *Acta Materialia* 60, 3655–3666.

Haefeli, R., Jaccard, C., de Quervain, M., 1968. Deformation of polycrystalline ice under combined uniaxial and hydrostatic pressure. International Association of Scientific Hydrology Publication 79 (General Assembly of Bern 1967 – Snow and Ice) , 341–344.

Hahn, H., Gleiter, H., 1979. The effect of pressure on grain growth and boundary mobility. *Scripta Metallurgica* 13, 3–6.

Hamann, C., Weikusat, I., Azuma, N., Kipfstuhl, S., 2007. Evolution of ice crystal microstructure during creep experiments. *Journal of Glaciology* 53, 479–489.

Helgerud, M., Waite, W.F., Kirby, S., Nur, A., 2009. Elastic wave speeds and moduli in polycrystalline ice Ih, sI methane hydrate, and sII methane hydrate. *Journal of Geophysical Research* 114, B02212.

Higashi, A., Sakai, N., 1961. Movement of small angle boundary of ice crystal. *Journal of the Faculty of Science, Hokkaido University. Ser. 2, Physics V*, 221–237.

Hirth, J., Lothe, J., 1982. *Theory of Dislocations*. 2nd ed., Wiley-Interscience.

Hobbs, P.V., 1974. *Ice Physics*. Oxford: Clarendon Press.

Hondoh, T., 2000. Nature and behavior of dislocations in ice, in: Hondoh, T.

(Ed.), *Physics of Ice Core Records*. Hokkaido University Press, Sapporo, pp. 3–24.

695 Hondoh, T., 2009. An overview of microphysical processes in ice sheets: Toward nanoglaciology, in: Hondoh, T. (Ed.), *Physics of Ice Core Records II*. Hokkaido University Press. volume 68.

Hondoh, T., 2013. Personal Communication.

Hondoh, T., Azuma, K., Higashi, A., 1987. Self-interstitials in ice. *Le*  
700 *Journal de Physique Colloques* 48, 183–187.

Iliescu, D., Baker, I., Chang, H., 2004. Determining the orientations of ice crystals using electron backscatter patterns. *Microscopy Research and Technique* 63, 183–187.

Jacka, T., Maccagnan, M., 1984. Ice Crystallographic and Strain Rate  
705 Changes with Strain in Compression and Extension. *Cold Regions Science and Technology* 8, 269–286.

Jessell, M., 1987. Grain-boundary migration microstructures in a naturally deformed quartzite. *Journal of Structural Geology* 9, 1007–1014.

Jones, S., Chew, H., 1983a. Creep of ice as a function of hydrostatic pressure.  
710 *The Journal of Physical Chemistry* 87, 4064–4066.

Jones, S., Chew, H., 1983b. Effect of Sample Size on the Compressive Strength of Ice. *Annals of Glaciology* 4, 129–132.

- Landgon, T., 1973. Creep Mechanisms in Ice, in: Whalley, E., Jones, S., Gold, L. (Eds.), *Physics and chemistry of ice: Symposium on the Physics and Chemistry of Ice*, Ottawa, Canada, 14-18 August 1972, pp. 356–361.
- 715
- Liu, F., Baker, I., Dudley, M., 1993. Dynamic observations of dislocation generation at grain boundaries in ice. *Philosophical Magazine A* 67, 1261–1276.
- Liu, F., Baker, I., Yao, G., Dudley, M., 1992. Dislocations and grain boundaries in polycrystalline ice: a preliminary study by synchrotron x-ray topography. *Journal of Materials Science* 27, 2719–2725.
- 720
- Lothe, J., Hirth, J., 1967. Dislocation Climb Forces. *Journal of Applied Physics* 38, 845–848.
- Louchet, F., 2004. Dislocations and plasticity in ice. *Comptes Rendus Physique* 5, 687–698.
- 725
- Margevicius, R., Lewandowski, J., 1991. The effects of hydrostatic pressure on the mechanical behavior of NiAl. *Scripta Metallurgica et Materialia* 25, 2017–2022.
- Mizuno, Y., 1992. High temperature creep of polycrystalline ice under hydrostatic pressure. *Physics and Chemistry of Ice*, Hokkaido University Press, Sapporo , 434–439.
- 730
- Mohamed, F.A., Langdon, T.G., 1974. Method of estimating stacking-fault energies in alkali halide crystals using creep data. *Journal of Applied Physics* 45, 1965–1967.

- 735 Nabarro, F., 2006. Creep in commercially pure metals. *Acta Materialia* 54, 263–295.
- Obbard, R., Baker, I., Sieg, K., 2006. Using electron backscatter diffraction patterns to examine recrystallization in polar ice sheets. *Journal of Glaciology* 52, 546–557.
- 740 Olson, E., 2011. Particle shape factors and their use in image analysis part 1: Theory. *Journal of GXP Compliance* 15, 85.
- Passchier, C.W., Trouw, R.A., 2005. *Microtectonics*. 2nd ed., Springer Verlag.
- Petrenko, V.F., Whitworth, R.W., 1999. *Physics of ice*. Clarendon Press.
- 745 Poirier, J., 1976. On the symmetrical role of cross-slip of screw dislocations and climb of edge dislocations as recovery processes controlling high-temperature creep. *Revue de Physique Appliquee* 11, 731–738.
- Poirier, J.P., 1985. *Creep of crystals: High-temperature deformation processes in metals, ceramics and minerals*. Cambridge University Press.
- 750 Rigsby, G.P., 1958. Effect of hydrostatic pressure on velocity of shear deformation of single ice crystals. *Journal of Glaciology* 3, 273–278.
- Schindelin, J., Arganda-Carreras, I., Frise, E., Kaynig, V., Longair, M., Pietzsch, T., Preibisch, S., Rueden, C., Saalfeld, S., Schmid, B., Tinevez, J.Y., White, D.J., Hartenstein, V., Eliceiri, K., Tomancak, P., Cardona,  
755 A., 2012. Fiji: an open-source platform for biological-image analysis.

Nature Methods 9, 676–682. URL: <http://dx.doi.org/10.1038/nmeth.2019>, doi:10.1038/nmeth.2019.

Schulson, E.M., Duval, P., 2009. Creep and Fracture of Ice. Cambridge University Press.

760 Sherby, O., Robbins, J., Goldberg, A., 1970. Calculation of Activation Volumes for Self-Diffusion and Creep at High Temperature. Journal of Applied Physics 41, 3961–3968.

Sherby, O.D., Burke, P.M., 1968. Mechanical behavior of crystalline solids at elevated temperature. Progress in Materials Science 13, 323  
765 – 390. URL: <http://www.sciencedirect.com/science/article/pii/0079642568900248>, doi:10.1016/0079-6425(68)90024-8.

Syrenko, A., Klinishev, G., Khoi, V., 1973. Recrystallization of copper under hydrostatic pressure up to 15 kbar. Journal of Materials Science 8, 765–769.

770 Tanner, L., Radcliffe, S., 1962. Effect of hydrostatic pressure on the kinetics of recrystallization in high-purity copper. Acta Metallurgica 10, 1161–1169.

Taubenberger, R., Hubmann, M., Granicher, H., 1973. Effect of hydrostatic pressure on the dielectric properties of ice  $I_h$  single crystals, in: Whalley, E. (Ed.), Symposium on the Physics and Chemistry of Ice, Royal Society  
775 of Canada, Ottawa, Ontario. pp. 194–198.

Treverrow, A., Budd, W., Jacka, T., Warner, R., 2012. The tertiary creep

- of polycrystalline ice: experimental evidence for stress-dependent levels of strain-rate enhancement. *Journal of Glaciology* 58, 301–314. doi:10.3189/2012JcG11J149.
- 780
- Trickett, Y., Baker, I., Pradhan, P., 2000. The orientation dependence of the strength of ice single crystals. *Journal of Glaciology* 46, 41–44.
- Tyson, W., 1971. Elastic Strain Energy of Dislocations in Ice. *Canadian Journal of Physics* 49, 2181–2186.
- 785 Ueki, M., Horie, S., Nakamura, T., 1987. Factors affecting dynamic recrystallization of metals and alloys. *Materials Science and Technology* 3, 329–337.
- Weertman, J., 1965. Theory of the Influence of Stacking-Fault Width of Split Dislocations on High-Temperature Creep Rate. *Transactions of the Metallurgical Society of AIME* 233, 2069–2075.
- 790
- Weertman, J., 1968. Dislocation Climb Theory of Steady-State Creep. *Transactions of the American Society for Metals* 61, 681–694.
- Weertman, J., 1973. Creep of Ice, in: Whalley, E., Jones, S., Gold, L. (Eds.), *Physics and chemistry of ice: Symposium on the Physics and Chemistry of Ice*, Ottawa, Canada, 14-18 August 1972, pp. 320–337.
- 795
- Weikusat, I., De Winter, D., Pennock, G., Hayles, M., Schneijdenberg, C., Drury, M., 2011. Cryogenic EBSD on ice: preserving a stable surface in a low pressure SEM. *Journal of Microscopy* 242, 295–310.